*Earth Planets Space*, **60**, 809–819, 2008

# In-situ stress at the northern portion of the Chelungpu fault, Taiwan, estimated on boring cores recovered from a 2-km-deep hole of TCDP

Yasuo Yabe[1], Sheng-Rong Song[2], and Chien-Ying Wang[3]

[1]*Observation Center for Prediction of Earthquakes and Volcanic Eruptions, Graduate School of Science, Tohoku University, Sendai 980-8578, Japan*
[2]*Department of Geosciences, National Taiwan University P. O. Box 13-318, Taipei, 106 Taiwan*
[3]*Institute of Geophysics, National Central University, No. 300, Jhongda Rd., Jhongli, 32001 Taiwan*

(Received November 13, 2006; Revised July 9, 2007; Accepted May 17, 2008; Online published September 8, 2008)

We have investigated the depth variation in the stress state at the northern part of the Chelungpu fault, Taiwan, which slipped during the 1999 Chi-Chi earthquake ($M_w$ 7.6). In-situ stress around the fault was estimated based on the stress memory of rocks recovered from five depths (739–1316 m) of a 2-km-deep-hole. The borehole intersects a fault zone at a depth of 1111 m (FZ1111), which is the best candidate for the Chelungpu fault. Our main results are: (1) the $S_{H_{max}}$ direction is parallel to the slip for the Chi-Chi earthquake and agrees with those of the local, regional, or tectonic scales estimated from various stress indicators; (2) significant aspects of the stress field are identical to those of paleostress; (3) the horizontal differential stress was significantly reduced just above FZ1111, which may be attributable to the existence of a significantly deformable zone at this depth.
**Key words:** 1999 Chi-Chi earthquake, Chelungpu fault, TCDP, crustal stress, stress memory, core method.

## 1. Introduction

Since crustal stress drives the fault motion, and its distribution affects the distribution of slip on the fault, an investigation of the state of in-situ stress near a fault provides key information to understanding faulting mechanics. An elucidation of the strength of faults is also very important as part of any investigation into the deformation processes of the earth's crust, as the former may control the strength of the crust. Fault strength can be directly determined by measuring crustal stress near the fault. Zoback *et al*. (1987), for example, estimated the stress state around the San Andreas fault in central California to find that the direction of maximum horizontal compression ($S_{H_{max}}$) is nearly normal to the fault. Sato *et al*. (2003) measured in-situ stress near the Nojima fault, central Japan and showed that the shear stress acting on the fault is significantly small. These results suggest that these faults are weak. In contrast, Scholz (2000) claimed that fault-normal compression in central California is a result of active folding in this area. He found that the $S_{H_{max}}$ direction in southern California has an angle of 30–60° to the San Andreas fault, implying that the fault is strong. Consequently, despite its importance, the fault strength remains unresolved.

The Chelungpu fault, Taiwan, is a shallow dipping (∼30°) thrust fault, which slipped during the 1999 Chi-Chi earthquake ($M_w$ 7.6). The observed surface exposure along the fault trace was 80 km in length, and the maximum vertical offset was found to be as large as 9 m (e.g., Kao and Chen, 2000; Lee *et al*., 2001). The dense strong-motion and GPS networks operating around the fault recorded interesting phenomena related to this large thrust earthquake. For example, Oglesby and Day (2001) reported an asymmetric distribution of surface deformation wherein the displacement of the hanging-wall was several times larger than that of footwall. They performed numerical simulations to show that this state can arise as a consequence of the interaction between the shallow dipping thrust fault and the earth's free surface. The wealth of information obtained by the dense networks of seismic stations has facilitated integrated and detailed analyses of the faulting process for this earthquake. Ma *et al*. (2001) and Zeng and Chen (2001) determined that a large slip with a long rise time occurred at a shallow part in the northern segment of the fault. Brodsky and Kanamori (2001) explained this behavior by elastohydrodynamic lubrication of the fault. Further, the slip vector was rotated from a mostly pure reverse faulting one to an oblique reverse faulting with significant left-lateral component during the rupture propagation from south to north. Wu *et al*. (2001) proposed that the rotation of the slip vector was caused by a complicated spatial variation in tectonic stress.

The Taiwan Chelungpu-fault Drilling Project (TCDP) was initiated to gain an understanding of the effect of the faulting and rupture processes of the Chelungpu fault on the Chi-Chi earthquake from a material science perspective. Deep drilling to a depth of 2 km was carried out 5 years after the earthquake at a site located on the hanging-wall of the northern part of the fault (Fig. 1) where the large slip region was estimated. Since the distance from the surface trace of the Chelungpu fault to the drilling site is about

Copyright © The Society of Geomagnetism and Earth, Planetary and Space Sciences (SGEPSS); The Seismological Society of Japan; The Volcanological Society of Japan; The Geodetic Society of Japan; The Japanese Society for Planetary Sciences; TERRAPUB.

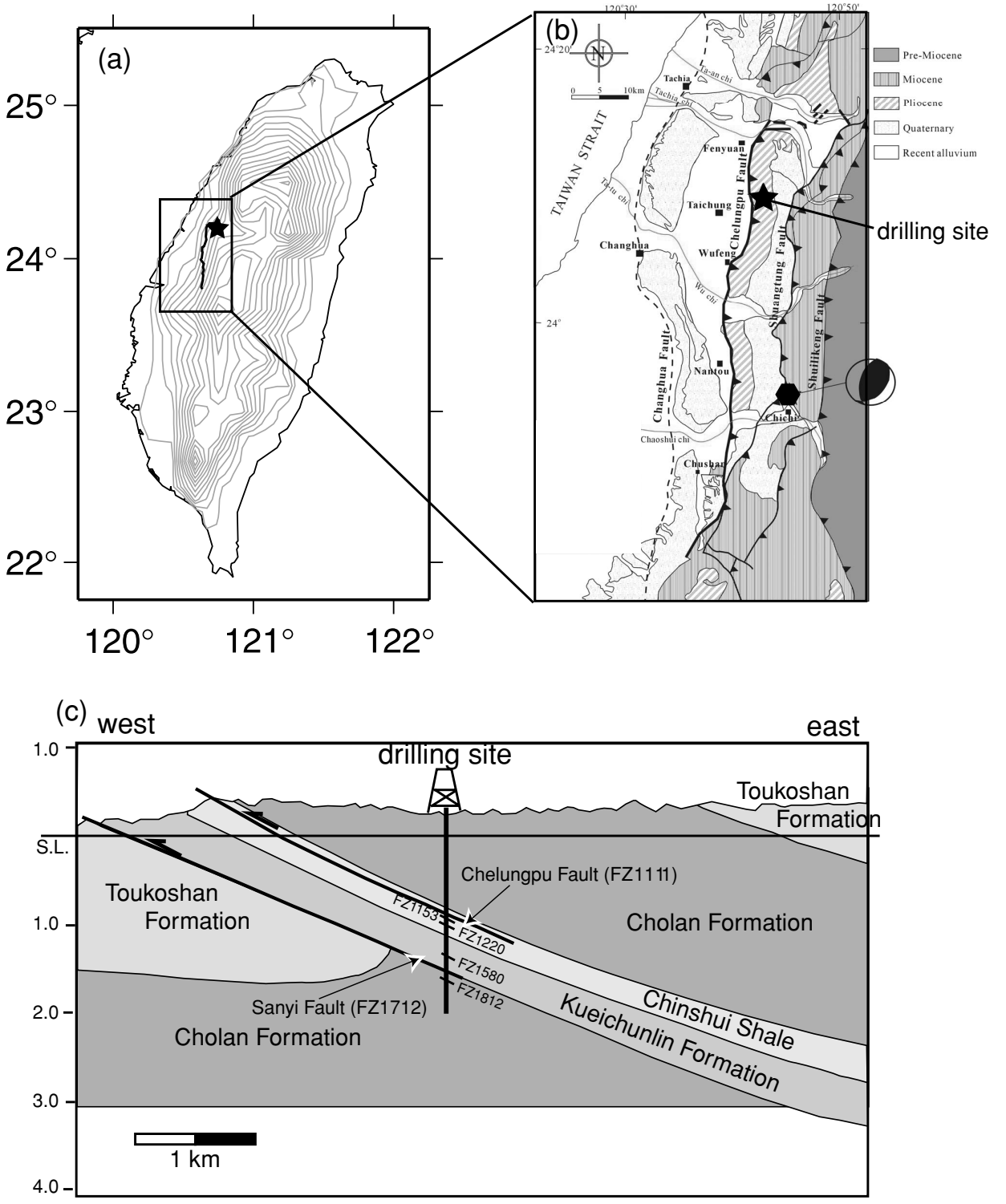


Fig. 1. (a) Map showing the Chelungpu fault trace (thick line) on the island of Taiwan. (b) Geological map showing surface rupture of the Chelungpu fault (thick line) associated with the 1999 Chi-Chi earthquake. (c) Schematic E-W cross section representing the relation among the fault zones, the stratigraphy and the major faults around the drilling site. Stars in (a) and (b) indicate the TCDP site. Hexagon in (b) represents the epicenter of 1999 Chi-Chi earthquake. (b) and (c) are modified from Song *et al*. (2007).

2 km, it was expected that the drilled hole should intersect the Chelungpu fault at a depth of about 1 km. At least six significant fault zones were found at depths of 1111 m (FZ1111), 1153 m (FZ1153), 1220 m (FZ1220), 1580 m (FZ1580), 1712 m (FZ1712), and 1812 m (FZ1812) (e.g., Song *et al*., 2007). However, pseudotachylyte was observed only in FZ1111, indicating that the dynamic slip occurred in FZ1111. Kano *et al*. (2006) carried out temperature logging around FZ1111 and found a thermal anomaly, indicating recent activation of this fault zone. Tanaka *et al*. (2007), however, reported that the thermal anomaly detected by Kano *et al*. (2006) should be caused by depth variations in thermal

conductivity. Based on these results, from the point of view of material science it can be considered that FZ1111 is the best candidate for the Chelungpu fault, which was activated for the 1999 Chi-Chi earthquake, while further investigations are required to determine this definitively.

We report here our investigation of the state of the in-situ stress around the Chelungpu fault on the basis of the stress memory of rocks. The so-called core methods were applied to cores collected from five depths of the TCDP hole. The main purpose of this study is to the constrain faulting process for the Chi-Chi earthquake from the perspective of the stress state.

## 2. Method

### 2.1 Outline of the techniques

There are many techniques that can be used to estimate the crustal stress. These are divided into two categories: (1) on-site methods, including the hydrofracturing test and the stress relief; (2) core methods, based on the stress memory of rocks, which is the ability of rocks to accumulate, retain and, under certain conditions, reproduce information on the stress history (Lavrov, 2003). Although the principle of on-site methods is clear, it is sometimes hard to apply these methods to such a deep hole as that drilled by the TCDP due to technical difficulties. In addition, such methods require a lot of time and money. We therefore applied three techniques of the core method to estimate the crustal stresses around the Chelungpu fault: (1) deformation rate analysis (DRA; Yamamoto *et al.*, 1990, 1993; Yamamoto, 1995), acoustic emission rate analysis (AERA; Yabe, 2004; Yabe *et al.*, 2004), and the AE method (Kanagawa *et al.*, 1977). All three techniques can be simultaneously applied to a single specimen under uniaxial cyclic loading. The main difference among these is the method used to evaluate the inelastic behavior of the specimen relating to the stress memory.

It is sometimes argued whether the stress memory of rock actually exists. The principal mechanisms of the AE method and DRA have been discussed in detail by Holcomb (1993) and Yamamoto (1995), respectively. Holcomb (1993) proposed that relaxation cracks would be generated when the core sample was retrieved from a depth, and AE activity may be generated by the closure of these cracks whose surface is perpendicular to the loading axis of the uniaxial compression test. Yamamoto (1995) makes the assumption that the nonuniformity in the stress distribution in rocks is minimized at sites and, on the basis of theory, concluded that the magnitude of the in-situ stress can be reproduced from the inelastic behavior of rocks, even if it is measured under the uniaxial compression test. In a practical setting, Villaescusa *et al.* (2002) demonstrated that the stress states estimated by both DRA and AE methods under varying geological environments are in good agreement with those obtained by the conventional overcoring method.

### 2.2 Preparation of specimens

Specimens having sizes of $12\times12\times32$ mm$^3$ were cut from the TCDP cores (Fig. 2) for the reconstruction of the axial stress embedded parallel to the long axis. Two pairs of strain gauges and two piezoelectric transducers (PZT) were attached onto the free surfaces of each specimen. As we

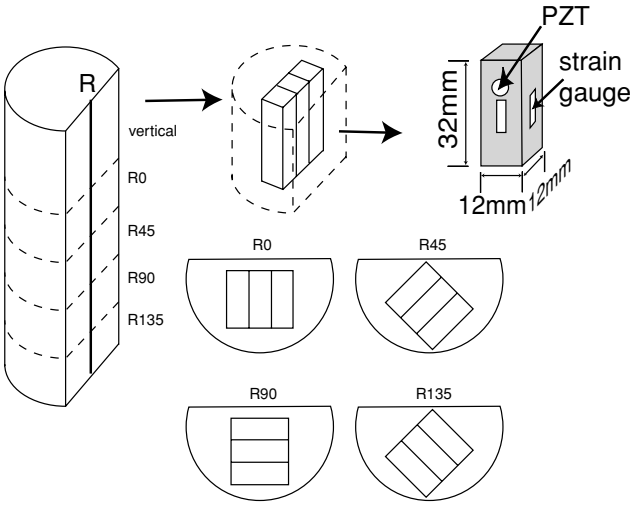


Fig. 2. Schematic illustration of the method employed for sample preparation in the present study. A set of specimens is first cut from a core sample. R indicates the reference azimuth of the core sample, which is taken perpendicular to the bedding direction.

took the average of the strain data obtained by two pairs of gauges on an analogue circuit, we recorded only one time series of strain. We did, however, separately record AE data measured by individual PZT transducers. The identification number of 1 or 2 was assigned to each PZT transducer to distinguish the time series of AE activities.

We assumed that one of the principal axes of the crustal stress is vertical; then we estimated the vertical and horizontal stresses in four directions at 45° intervals. We prepared three specimens in each direction and assigned identification numbers from 1 to 3 for convenience so that individual specimens could be provided with their own name in a form of TCDP*dddd*-V-*s* for the vertical specimens or of TCDP*dddd-aaa-s* for the horizontal specimens, where *dddd*, *s* and *aaa* stand for the depth, the identification number of specimen and azimuth, respectively. For example, the first specimen cut from a core recovered from 739 m to estimate the vertical stress was designated TCDP0739-V-1.

### 2.3 Reading the stress memory

For the case of DRA, we detected the stress memory using the strain difference function: $\Delta\varepsilon_{ij}(\sigma) = \varepsilon_i(\sigma) - \varepsilon_j(\sigma)$, where $\sigma$ and $\varepsilon_k(\sigma)$ is the applied axial stress and the axial strain for $k$-th loading, respectively, and $i > j$. The stress memory is recognized as a discontinuous change in the gradient (bending) of this function, as schematically shown in Fig. 3(a). In the ideal case (top function in Fig. 3(a)), the function has only one bending. However, since the function is sensitive to fluctuation in stress rate, it is sometimes bent twice or more by a small fluctuation in ram stroke of the loading apparatus (second to fifth functions in Fig. 3(a)). The stress rate in different loading cycles does not necessarily fluctuate at the same magnitude of applied stress. We also estimated the magnitude of memorized stress in each azimuth using at least two specimens. The magnitudes of applied stress at which the bending of the function due to the fluctuation in stress rate occurs should depend on the combination of loading cycles ($i$ and $j$) used to calculate the strain difference function and the specimen. On the other

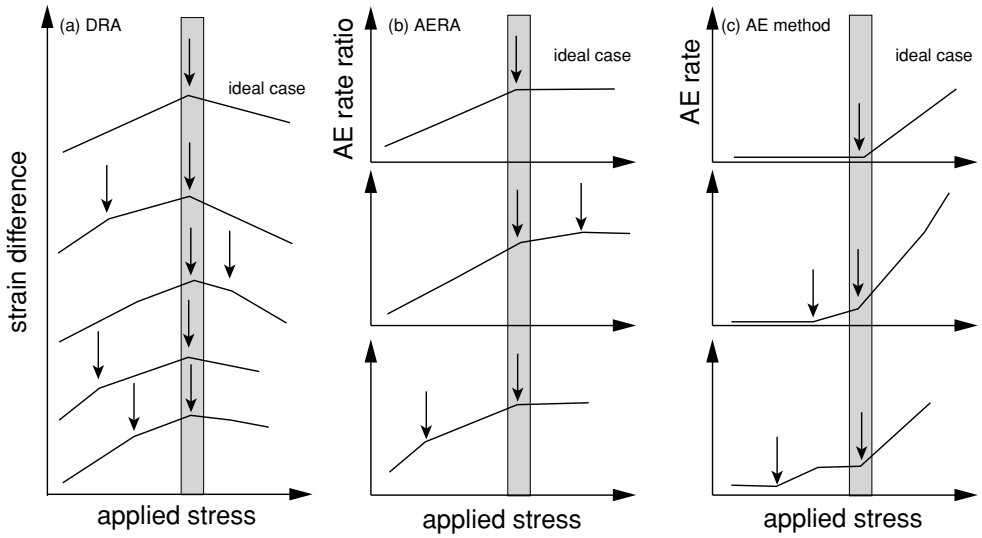


Fig. 3. Schematic illustration of (a) the strain difference function, (b) the AE rate ratio function, and (c) the relationship between applied stress and AE rate. Arrows indicate the inelastic behavior of functions. Shaded area represents a stress magnitude range in which the inelastic behavior commonly observed on all of the strain difference functions, the AE rate ratio functions, and the relationship between applied stress and AE rate.

hand, the magnitude of applied stress at which the bending representing the stress memory occurs does not depend on either the loading cycles or the specimens, as shown in the shaded area in Fig. 3(a).

Since, in our experience, the AE activity is less affected by the fluctuation in stress rate, we employed the AE method and AERA in addition to DRA. The outputs of the PZT transducers are rectified by analog circuits to obtain the envelope. The envelopes for the first and the second loading cycles are recorded continuously at a sampling frequency of 100 kHz. AE events with peak amplitudes greater than a threshold value are discriminated from the envelope data after the completion of the experiment. The threshold amplitude to discriminate AE was set by trial and error. The threshold amplitude for AERA is typically as small as 1.5- to 2-fold the noise level, while it is typically three- to fourfold that of the noise level in the AE method.

In case of the AERA, the stress memory is reproduced from the AE rate ratio function: $\mathrm{ARR}(\sigma) = N_1(\sigma)/N_2(\sigma)$, where $N_k(\sigma)$ is the AE rate for the $k$-th loading. The function is convex in nature, and the magnitude is generally less than unity. The stress memory can be recognized as a discontinuous change in the gradient of the function, as schematically illustrated in Fig. 3(b). In an ideal case (top panel of Fig. 3(b)), the gradient changes only at the magnitude of applied stress corresponding to the memorized stress.

For the AE method, the stress memory is evaluated from the non-linear relationship between the magnitude of applied axial stress and the occurrence rate of large AE events during the first loading, as schematically shown in Fig. 3(c). In an ideal case (top panel), AE activity is insignificant when the magnitude of applied stress is low, but it increases rapidly once the applied stress reaches a critical value. This critical value of the applied stress corresponds to the magnitude of stress embedded in the specimen.

AE activity is sometimes contaminated by such noises as the occurrences of AE events that do not relate to the stress memory or the instability of the ground potential of the measurement system. As a result, the gradient of AE rate ratio function is sometimes changed twice or more. An increase in AE that is not related to the stress memory is occasionally observed in the AE method. However, the perturbations on the outputs of two transducers differ from one another as long as AE activity that does not relate to the stress memory is localized. The instability of the ground potential varies from one circuit to another. Further, these phenomena are not necessarily reproduced in another specimen. Thus, the magnitude of applied stress at which AE activity relating to stress memory is contaminated by noises depends on both the transducer and specimen. Conversely, the change in AE activity relating to the stress memory must occur at a particular magnitude of applied stress independent of either the transducer or specimen, as schematically shown in shaded area in Figs. 3(b) and (c).

In addition to the contamination by noises stated above, the inelastic behavior relating to the stress memory is sometimes unclear due to the presence of other factors. The change in the gradient of strain difference function and/or AE rate ratio function is minor. The increase in the occurrence rate of large AE events is gradual rather than steep. One possible reason for these observations can be that the magnitude of the maximum applied stress is either too large or too small. At least two specimens in each azimuth must be tested under different magnitudes of the maximum stress.

In summary, we cannot determine the stress memory of rocks from individual functions; they must be surveyed in combination. We applied the following constraints in determining the stress memory: (1) the magnitude of the memorized stress does not depend on the maximum applied stress; (2) the magnitude of memorized stress does not depend on the estimation technique; (3) for DRA, the magnitude of memorized stress does not depend on the combinations of loading cycles; (4) for AERA and AE method, the magnitude of memorized stress does not depend on the PZT

transducer; (5) the magnitude of vertical stress does not significantly differ from the overburden pressure; (6) the dependence of horizontal stress on azimuth obeys a sinusoidal function; $\sigma(\theta) = \sigma_m + \sigma_a \cos(2(\theta - \theta_0))$, where $\theta$ is the azimuth, $\theta_0$ is the azimuth of the maximum horizontal compression, and $\sigma_m$ and $\sigma_a$ represent the magnitudes of the isotropic and deviatoric components of horizontal stress, respectively.

## 3. Results

Figure 4 shows a typical loading history and the stress-strain relationship obtained from a vertical specimen of 739 m depth. The loading rate was 0.1 MPa/s. There were five or seven loading cycles, depending on the quality of data. As it was expected that the stress state in the crust tends toward the lithostatic state, we assumed that the magnitudes of horizontal stress do not significantly differ from the vertical stress. We therefore did not carry out tests with the maximum stress larger than threefold the vertical stress.

Figure 5 shows the strain difference function, the AE rate ratio function, and the dependence of large AE rate on stress for vertical specimens at a depth of 739 m. The expected overburden pressure at this depth is 17.4 MPa for a density of 2400 kg/m$^3$, which is the average density measured by logging. The only one bending occurs at about 18 MPa in both $\varepsilon_{35}$ of specimen TCDP0739-V-1 and $\varepsilon_{45}$ of specimen TCDP0739-V-2, which is close to the expected overburden pressure. There are two significant bendings in $\varepsilon_{34}$ of specimen TCDP0739-V-1 at about 16 MPa and about 23 MPa, respectively. The latter is much larger than the expected overburden pressure. Two bendings at about 12 MPa and 18 MPa are found also in $\varepsilon_{34}$ of specimen TCDP0739-V-2. The former is too small compared with the expected overburden pressure. The shaded area in Fig. 5(a) indicates a stress magnitude of 18±2 MPa. The above four functions have bending in this stress range. The $\varepsilon_{23}$ of specimen TCDP0739-V-2 bends at about 14 MPa, and although this is slightly smaller than the stress magnitude at which bendings in other functions occurred, the bending is relatively clear. Consequently, we consider this bending to be possibly related to the stress memory. The gradient of the AE rate ratio function (ARR) obtained by PZT2 of specimen TCDP0739-V-1 (Fig. 5(b)) changes at about 18 MPa, while that obtained by PZT2 of specimen TCDP0739-V-2 (Fig. 5(c)) changes twice, at about 14 MPa and 20 MPa. Although the significances of the two gradient changes are similar, the latter is more consistent with the stress magnitude at which inelastic behavior is observed on other data. The AE rate observed by PZT2 of specimen TCDP0739-V-1 (Fig. 5(d)) and by PZT1 of specimen TCDP0739-V-2 (Fig. 5(e)) increased at about 18 MPa and 16.5 MPa, respectively. These values are consistent with the stress magnitudes estimated by DRA and AERA. We therefore estimated the magnitude of vertical stress to be about 18 MPa.

Figure 6 shows the strain difference function, the AE rate ratio function, and the dependence of large AE rate on stress for specimens in the reference azimuth at a depth of 739 m. Although there are two bendings in some of the strain difference functions, all strain difference functions have bending within a stress magnitude range of 16.5±2 MPa

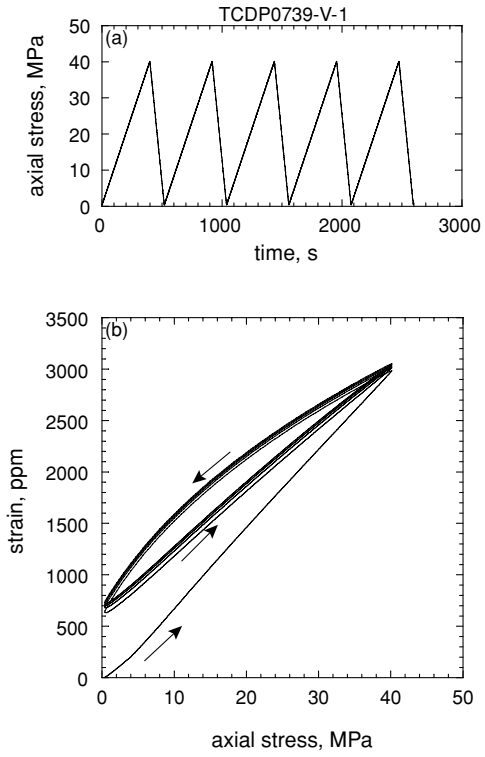


Fig. 4. Examples of (a) loading history and (b) a stress-strain curve for a vertical specimen at a depth of 739 m. Arrows in (b) indicate increase in time.

(shaded are in Fig. 6). The occurrence of large AE events also becomes significant when the applied stress exceeds this stress range. We therefore considered that the in-situ stress magnitude in this azimuth should be within this stress range. Although the gradient changes of ARR observed by PZT2 of TCDP0739-000-1 (Fig. 6(b)) and TCDP0739-000-2 (Fig. 6(c)) occur at about 13 MPa, being slightly smaller than the above stress range, we also adopted these inelastic behaviors as a representation of stress memory since they are clear.

Figure 7 presents the data for the azimuth of R45 at a depth of 739 m. All strain difference functions, ARR functions, and the applied stress dependences of AE rate indicate inelastic behavior within a stress range of 13±2 MPa (shaded area in the figure). We therefore regarded the inelastic behaviors within this stress range to be a representation of the stress memory.

Figure 8 is for specimens in the azimuth of R90 at 739 m depth. Except for the relationship between axial stress and AE rate observed by PZT2 of specimen TCDP0739-090-2 (Fig. 8(e)), inelastic behavior is observed on all functions within the stress range of 20±2 MPa. Non-linear behavior on the relationship between applied stress and AE rate observed by PZT2 of specimen TCDP0739-090-2 occurred at about 24 MPa. Since the increase in AE rate is relatively significant, we accepted this stress as the in-situ stress memorized in this specimen.

Figure 9 represents the strain difference function, the AE rate ratio function, and the dependence of large AE rate on stress for specimens in the azimuth of R135 at a depth of 739 m. All of the functions show inelastic behavior within a

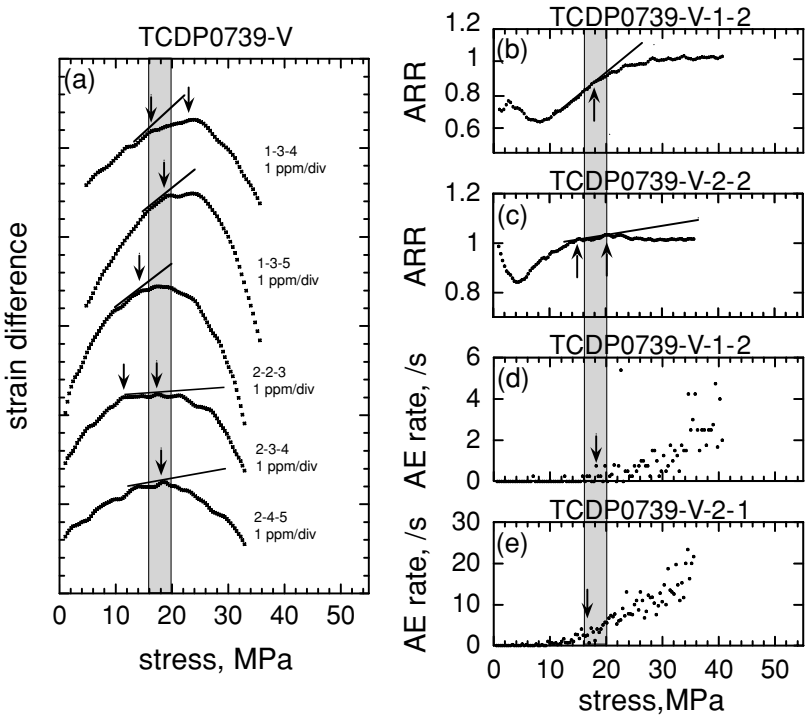


Fig. 5. Examples of (a) strain difference function, (b), (c) AE rate ratio function, and (d), (e) rate of occurrence of large AE events obtained for the same specimen as described in Fig. 4. The three digits beside the strain difference functions in (a) represent the specimen ID and sequential number of loading cycles used to obtain the functions. For example, 1-3-4 denotes the $\Delta\varepsilon_{34}(\sigma)$ of specimen 1. Characters above individual figures (b)–(e) indicate the specimen name and identification number of PZT used to obtain data shown in respective figures. For example, TCDP0739-V-1-2 means that the data were obtained by the second PZT on specimen of TCDP0739-V-1. Lines in (a) and (b) are drawn to emphasize changes in the gradients of functions. Arrows and shaded area are the same as in Fig. 3.

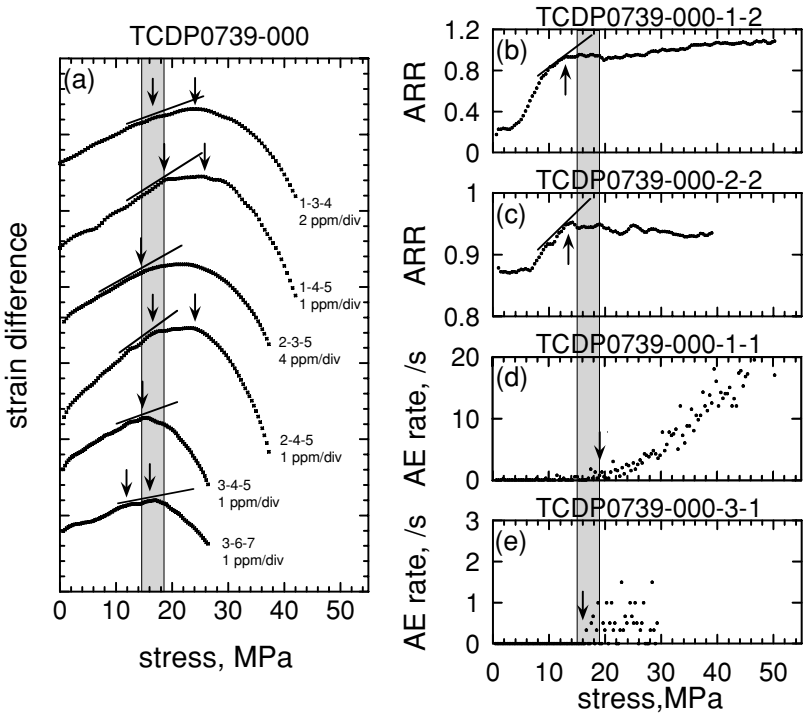


Fig. 6. Same as Fig. 5, but for horizontal specimens parallel to the reference direction at a depth of 739 m.

stress magnitude range of 23±2 MPa, although some strain difference functions have two bendings. We considered that inelastic behavior in this stress range represents the stress memory.

Up to this point we have only presented a rough range of the stress magnitude determined as the in-situ stress for the purpose of simplicity. The magnitude of the applied stress at which the inelastic behavior relating to the stress memory

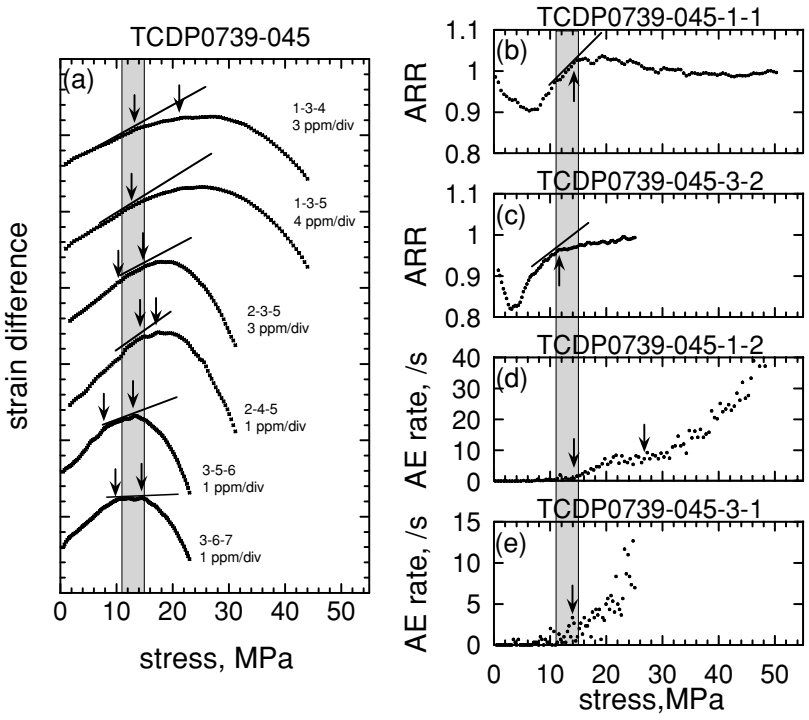


Fig. 7. Same as Fig. 5, but for horizontal specimens at an azimuth of 45° from the reference direction and at a depth of 739 m.

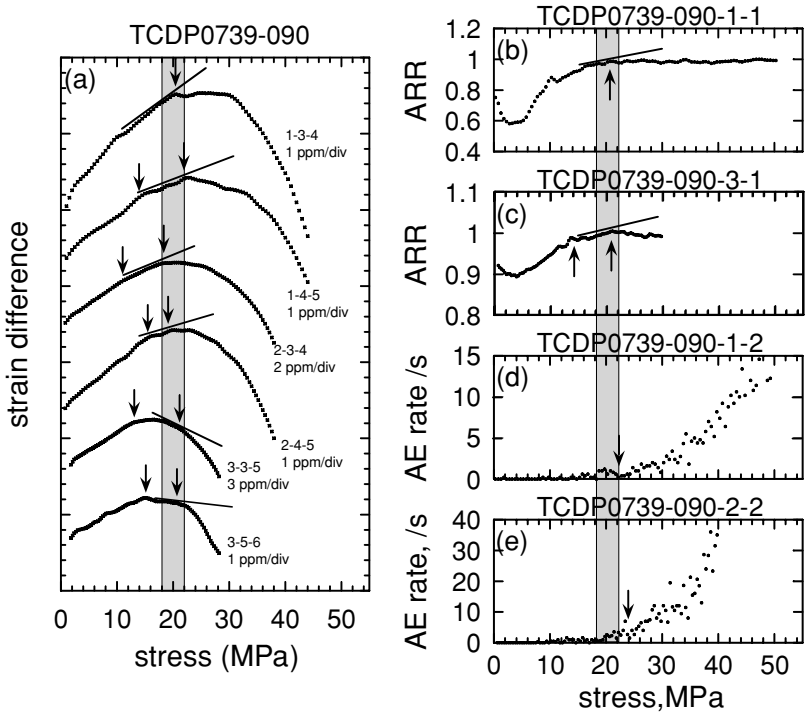


Fig. 8. Same as Fig. 5, but for horizontal specimens at an azimuth of 90° from the reference direction and at a depth of 739 m.

was found in each function was precisely measured in the following analyses.

The average difference between stresses estimated from different specimens in the same orientation was found to be about 2 MPa, which provides a rough estimate for the magnitude of the error in stress along each orientation. Figure 10 shows the azimuthal dependence of the stress magnitude estimated at a depth of 739 m. The error involved in fitting the sinusoidal function was 0.3–0.7 MPa for the isotropic component and 0.4–0.9 MPa for the deviatoric component. Thus, the overall error involved in estimating the magnitude of horizontal stress was 3–4 MPa in general. The cores were orientated by comparing the bedding observed on the core and the FMI image of the borehole. The accuracy of this process is estimated to be about 10°. Further, misalignment of cores in preparing the specimens can

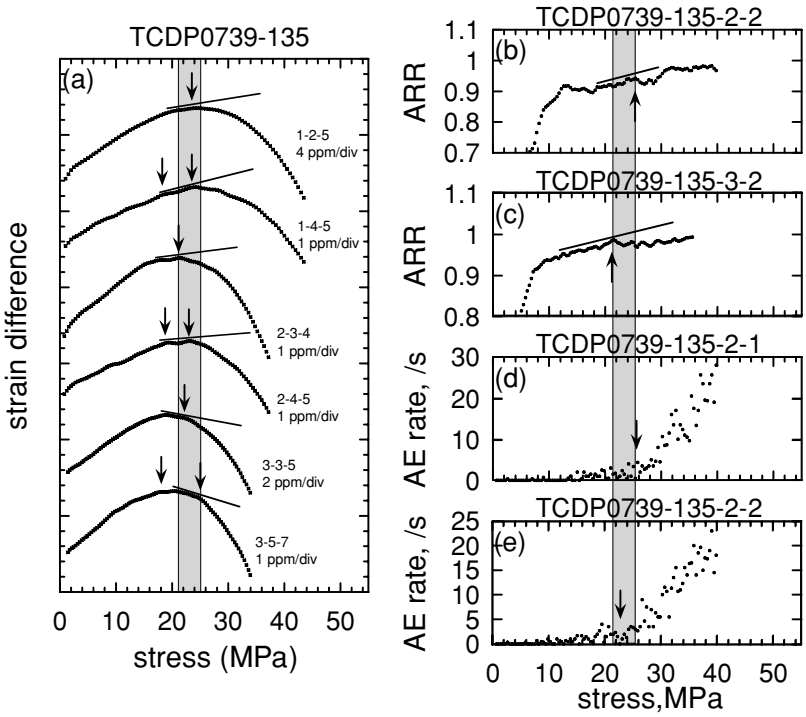


Fig. 9. Same as Fig. 5, but for horizontal specimens at an azimuth of 135° from the reference direction and at a depth of 739 m.

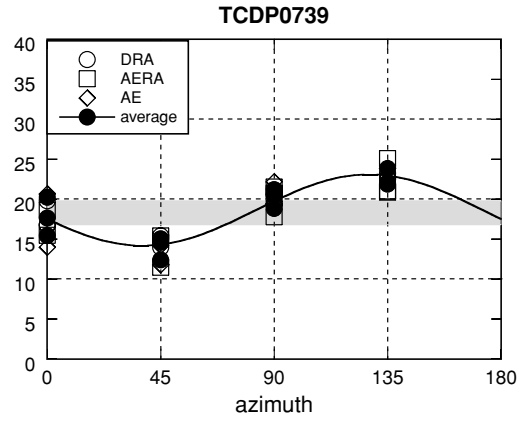


Fig. 10. Dependence of the estimated horizontal stress on azimuth at a depth of 739 m. Open circles, squares, and diamonds represent stress magnitudes derived from the DRA, AERA, and AE methods, respectively. Solid circles indicate the average values of stress magnitude estimated from the three methods for individual specimens. Solid line represents the best fit sinusoidal function to the average values. Shaded zone represents the range of the estimated vertical stress.

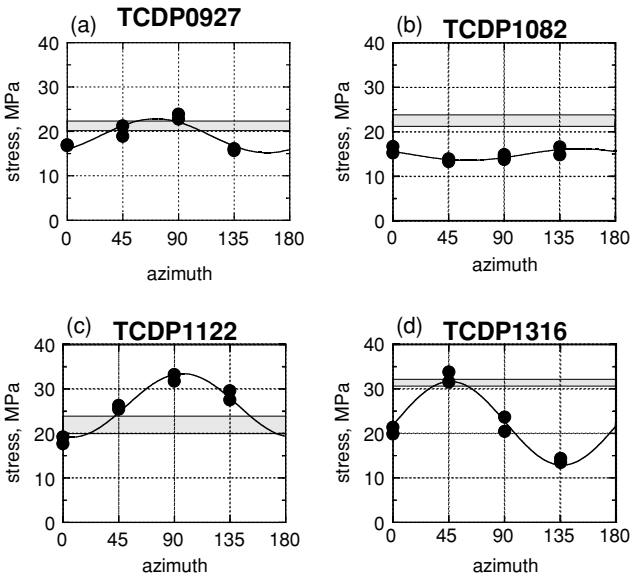


Fig. 11. Same as in Fig. 10, but for depths of (a) 927 m, (b) 1082 m, (c) 1122 m, and (d) 1316 m.

be 10–20°. Thus, the error in the azimuth of the maximum horizontal compression is 20–30°, whereas the error in fitting for $\theta_0$ is negligibly small ($\sim$1°).

Figure 11 shows the azimuthal dependence of stresses estimated at depths of 927 m, 1082 m, 1122 m, and 1316 m. Table 1 summarizes the estimated stress states with the lithology. Figure 12 shows the depth dependence of the magnitudes of principal stress. The rock densities from the surface to a depth of 1.3 km were measured by logging, and an average density of 2400 kg/m$^3$ was determined. We calculated a theoretical profile of vertical stress (dashed line in Fig. 12) using the logging data of density. The depth dependence of $S_v$ generally agrees well with the profile within the error, thereby showing the reliability of our estimation. Critical inspection, however, revealed that the gradient of $S_v$ seems to change at a depth of 1082 m. This may be related to the change in the stratum from the Cholan Formation to Chinshui Shale at a depth of 1029 m.

Both magnitudes of maximum ($S_{H_{max}}$) and minimum horizontal compressions ($S_{h_{min}}$) do not seem to increase linearly with depth. The magnitude of $S_{H_{max}}$ at a depth of 1082 m, which is just above FZ1111, was found to be significantly smaller than that at other depths and almost equal to $S_{h_{min}}$.

Table 1. Estimated stress state and geological information.

| Depth, m | $S_v$, MPa | $S_{H_{max}}$, MPa | $S_{h_{min}}$, MPa | $S_{H_{max}}$ azimuth† | Lithology | Stratum | Bedding direction |
|---|---|---|---|---|---|---|---|
| 739 | 18.2 | 23.1 | 14.2 | 146 | shale/siltstone | Cholan Fm. | N109E |
| 927 | 20.9 | 22.9 | 15.2 | 83 | strong bioturbated formation | Cholan Fm. | N099E |
| 1082 | 22.4 | 16.3 | 13.7 | 164 | strong bioturbated formation | Chinshui Shale | N102E |
| 1122 | 21.6 | 33.4 | 19.1 | 113 | strong bioturbated formation | Chinshui Shale | N112E |
| 1316 | 31.3 | 31.6 | 12.9 | 83 | sandstone | Kueichulin Fm. | N127E |

†The azimuth is measured clockwise from the north.

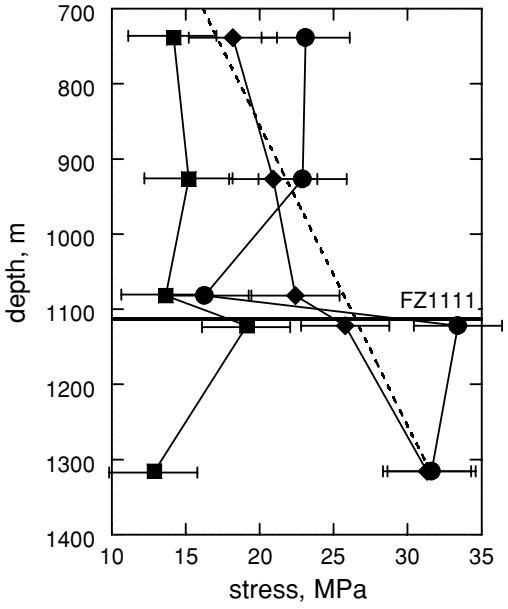


Fig. 12. Dependence of the magnitudes of the principal stress on depth. Solid diamonds, circles, and squares represent the vertical ($S_v$), the maximum horizontal ($S_{H_{max}}$), and the minimum horizontal ($S_{h_{min}}$) stresses, respectively. Dashed line shows the depth dependence of overburden pressure calculated from the logging data of density.

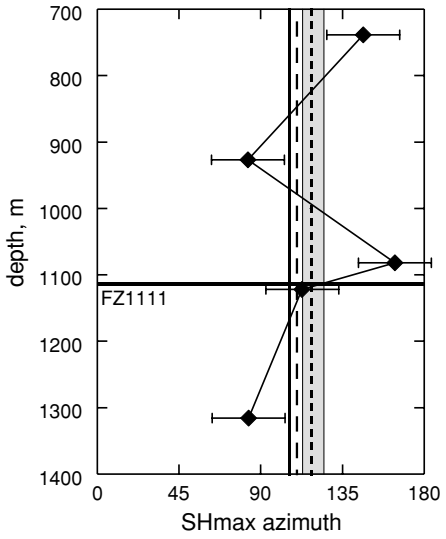


Fig. 13. Dependence of $S_{H_{max}}$ azimuth on depth. The azimuth is measured clockwise from the north. Short-dashed and solid lines represent the average azimuth of $S_{H_{max}}$ calculated with and without the datum of 1082 m depth, respectively. The long-dashed line shows the $S_{H_{max}}$ azimuth of paleostress. Shaded area represents the range of the coseismic slip direction of the Chi-Chi earthquake.

This will be handled in more detail in Discussion.

Figure 13 shows the depth dependence of the $S_{H_{max}}$ azimuth. Considering the relatively large errors in $S_{H_{max}}$ azimuth (∼20–30°), their values at individual depths are not significant. The average of the estimated azimuth of $S_{H_{max}}$ is N118E (short-dashed line in Fig. 13). Since the deviatoric component of horizontal stress at a depth of 1082 m is small, the reliability of the $S_{H_{max}}$ azimuth at this depth would be lower than that at other depths. When this data set is omitted, the average azimuth was found to be N106E (solid line in Fig. 13). In general, the strike of the Chelungpu fault is about N5E, while it is about N65E at the northernmost portion of the fault (Fig. 1). It can therefore be said that the average azimuth of $S_{H_{max}}$ is roughly normal to the general strike of the fault.

## 4. Discussion

### 4.1 Comparison with the in-situ stress state estimated by conventional methods

Two deep holes were drilled within the framework of the TCDP project: Hole-A, from which the core samples used in the present study were recovered, and Hole-B, which was drilled at several tens of meters from Hole-A. Wu *et al*. (2007) analyzed the borehole breakout observed by the logging of Hole-A. They estimated that the azimuth of $S_{H_{max}}$ is N115E, being parallel to the regional stress. Wu *et al*. (2005) and Hung *et al*. (2008) measured the *S*-wave anisotropy by wire-line logging in Hole-A and they found that, on average, the fast *S*-wave is polarized in the ESE-WNW direction. The $S_{H_{max}}$ axis can then be considered to be in this direction, if the *S*-wave anisotropy was caused by preferentially oriented cracks in the crust.

Hung *et al*. (2008) performed hydraulic fracturing test in Hole-B and estimated the magnitude of $S_{h_{min}}$ to be about 16 MPa. They also analyzed the borehole breakouts and the drilling induced tensile fractures in a depth range from 930 m to 1330 m in Hole-B and found that the $S_{H_{max}}$ direction is, on average, N120E or N130E, except for just above the Chelungpu fault.

The $S_{h_{min}}$ magnitude and $S_{H_{max}}$ azimuths determined from our study are nearly identical to those obtained by other researchers using conventional methods. We therefore conclude that the in-situ stress state around the Chelungpu fault was successfully reconstructed in our study on the basis of stress memory.

### 4.2 Comparison with the $S_{H_{max}}$ azimuth estimated from other indicators of the stress field

The island of Taiwan resulted from a collision between the Luzon arc belonging to the Philippine Sea plate and the Chinese continental margin of the Eurasian plate. As the

Philippine Sea plate moves in the direction of N60W relative to the Eurasian plate in the vicinity of Taiwan (Seno, 1977; Yu *et al.*, 1997), the $S_{H_{max}}$ azimuth of the tectonic stress in the island of Taiwan is expected to be oriented in a range between SE-NW and ESE-WNW. Rau *et al.* (1996) determined the focal mechanisms of small to moderate earthquakes occurring in the western Taiwan and the Central Range area from 1991 to 1994. They showed that the $P$-axis of the events generally lies in the direction of ESE-WNW, which is nearly parallel to the relative direction of plate motion, even though both strike-slip and thrust events also occurred. These results suggest that the regional or tectonic stress field on the scale of the island of Taiwan is dominated by the ESE-WNW compression. Thus, the $S_{H_{max}}$ azimuth estimated in this study is in agreement with the expected direction of tectonic compression on a regional scale.

Angelier *et al.* (1986) analyzed fault-slip and fold patterns in the western Taiwan for reconstructing the paleostress field for the last 2–3 Ma. They showed that the axis of maximum compression was horizontal during the Quaternary and that its azimuth was about N110E (long-dashed line in Fig. 13) in the central part of western Taiwan, where the Chelungpu fault exists. Further, the axis of intermediate compression dipped close to the vertical during this period. The present stress field around the Chelungpu fault, as estimated in this study, is similar in some aspects to the paleostress field. That is, the maximum and intermediate principal compressions were horizontal and vertical, respectively. Further, the $S_{H_{max}}$ azimuth of N106E approximates that of the paleostress. The major difference between the present stress and the paleostress fields is in the relative magnitudes of the principal compressions. The present magnitude of $S_v$ is significantly larger than that of minimum compression ($S_{h_{min}}$), while those in the case of paleostress were estimated to be nearly equal to each other.

### 4.3 Implication for the faulting process of the 1999 Chi-Chi earthquake

Although it is known from the CMT solution estimated by USGS, Harvard, or Wu *et al.* (2001) that the Chi-Chi earthquake was a thrust faulting event, the vertical stress was not estimated as the minimum principal compression in our study. At depths of 739 m, 927 m and 1122 m, the $S_v$ is the intermediate principal compression, indicating that the stress state is of the strike-slip faulting type. The magnitudes of $S_{H_{max}}$ and $S_v$ are nearly equal to each other at a depth of 1316 m, implying the possibility of the occurrence of both strike-slip and normal faulting—if the weakness of the crust distributes randomly. Further, the stress state of the normal faulting regime is estimated at a depth of 1082 m proximately above the Chelungpu fault (FZ1111).

When the coseismic slip vector for the Chi-Chi earthquake is projected onto the horizontal plane, its azimuth ranges between N113E and N125E (shaded area in Fig. 13). This is parallel to the $S_{H_{max}}$ axis estimated in the present study. Further, as stated in the previous section, the $S_{H_{max}}$ axis is nearly perpendicular to the Chelungpu fault strike. In other words, the $S_{h_{min}}$ axis is parallel to the fault plane and perpendicular to the slip vector. This means that the fault motion for the Chi-Chi earthquake was not driven by the differential stress between the maximum compression ($S_{H_{max}}$) and the minimum compression ($S_{h_{min}}$), but by the differential stress between the maximum compression ($S_{H_{max}}$) and the intermediate compression ($S_v$). This result suggests that the fault motion for the Chi-Chi earthquake was controlled by the geometry of the weakness in the crust as well as by the stress state.

### 4.4 A possible cause of anomalous stress state just above the Chelungpu fault

Figure 14 shows the depth dependence of the Young's modulus estimated from the stress-strain curve for the case of the first loading. The Young's modulus takes a minimum value at a depth of 1082 m, proximately above the Chelungpu fault (FZ1111). Although the residual strain after the first loading was generally as large as 20–30% of the peak strain (Fig. 4(b)), the peak strain for the second loading was nearly equal to that for the first loading. As a result, Young's modulus estimated from the stress-strain curve for the second loading is significantly larger than that of the first loading. Although the residual strain is increased progressively by repetitive loading, the value of Young's modulus is stable after the second cycle. We calculated the increase rate of Young's modulus, $\Delta E = (E_a - E_1)/E_1$ for evaluating the deformability, where $E_1$ and $E_a$ is the Young's modulus of the first loading and the average of Young's moduli after the second loading, respectively. At a depth of 1082 m, the increase rate was found to be a maximum and as large as 75%. Both the small Young's modulus and the large increase rate at the 1082 m depth suggest the existence of a significantly deformable zone at this depth. This inference is supported by Ma *et al.* (2006) and Song *et al.* (2007), who reported the thickness of the damaged zone around FZ1111 to be wider in the hanging-wall than in the footwall by analyzing the TCDP core.

The deformable damaged zone can not sustain the differential stress, as observed by Sato *et al.* (2003) in the case

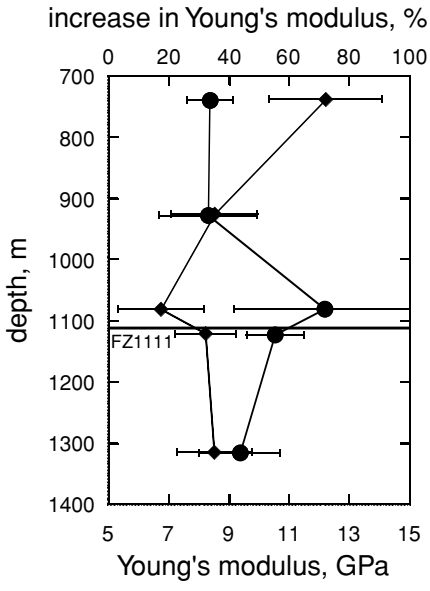


Fig. 14. Depth dependences of Young's modulus for the first loading (solid diamonds, bottom axis) and its increase rate, $\Delta E$ (solid circles, top axis).

of the Nojima fault, central Japan. If the deformable damaged zone extends along a fault plane, significant relaxation of differential stress in the damaged zone may occur, which will result in one of the principal axes being normal to the fault. In the case of the Chelungpu fault, as the $S_{h_{min}}$ axis is parallel to the fault plane, it would not be rotated by the relaxation of the differential stress in the deformable damaged zone. Further, the magnitude of $S_v$ would be constrained by the overburden pressure. Only $S_{H_{max}}$ can be perturbed by the deformation in the damaged zone. The small magnitude of $S_{H_{max}}$ at the proximity above the Chelungpu fault could be caused by the relaxed stress field in the damaged zone.

## 5. Conclusion

We estimated the stress state near the Chelungpu fault, which slipped at the Chi-Chi earthquake ($M_w$ 7.6) in 1999, using boring core samples retrieved from five depths of a 2-km deep hole drilled by the TCDP. Although more data are required to draw a definitive conclusion, there are three main results from this study. (1) the $S_{H_{max}}$ azimuth is N106E on average and is perpendicular to the strike of the Chelungpu fault and parallel to the coseismic slip vector of the Chi-Chi earthquake. Further, it agrees well with other indicators of stress field, such as focal mechanisms for small to moderate earthquakes in western Taiwan and the relative plate motion direction in the vicinity of the island of Taiwan. (2) The main aspects of the stress field, such as $S_{H_{max}}$ azimuth and orders of magnitude among $S_{H_{max}}$, $S_v$, and $S_{h_{min}}$ obtained in this study, are nearly identical to those of paleostress. (3) The magnitude of $S_{H_{max}}$ is significantly reduced at the proximity above the Chelungpu fault (FZ1111). This may be due to the relaxation of shear stress in the deformable damaged zone at this depth.

**Acknowledgments.** This research was partially supported by the Grant-in-Aid for Scientific Research No. 16253003. Discussions with Dr. En-Chao Yeh of National Taiwan University and Dr. Hisao Ito of JAMSTEC were helpful to us. Critical and constructive comments by two anonymous reviewers were useful in improving the manuscript.

## References

Angelier, J., E. Barrier, and H.-T. Chu, Plate collision and paleostress trajectories in a fold-thrust belt: The foothills of Taiwan, *Tectonophys.*, **125**, 161–178, 1986.

Brodsky, E. E. and H. Kanamori, Elastohydrodynamic lubrication of faults, *J. Geophys. Res.*, **106**, 16357–16374, 2001.

Holcomb, D. J., General theory of the Kaiser effect, *Int. J. Rock Mech. Min. Sci. Geomech. Abstr.*, **30**, 929–935, 1993.

Hung, J.-H., K.-F. Ma, C.-Y. Wang, H. Ito, W. Lin, and E.-C. Yeh, Subsurface structure, physical property, fault-zone characteristics and stress state in scientific drill holes of Taiwan Chelungpu Fault Drilling Project, *Tectonophys.*, doi:10.1016/j.tecto.2007.11.014, 2008 (in press).

Kanagawa, T., M. Hayashi, and N. Nakasa, Estimation of spatial geostress components in rock samples using the Kaiser effect of acoustic emission, *Proc. Jpn. Soc. Civil Eng.*, **285**, 63–75, 1977 (in Japanese).

Kano, Y., J. Mori, R. Fujio, H. Ito., T. Yanagidani, S. Nakao, and K.-F. Ma, Heat Signature on the Chelungpu Fault Associated with the 1999 Chi-Chi, Taiwan Earthquake, *Geophys. Res. Lett.*, **33**, doi:10.1029/2006GL026733, 2006.

Kao, H. and W.-P. Chen, The Chi-Chi earthquake sequence: active out-of-sequence thrust faulting in Taiwan, *Science*, **288**, 2346–2349, 2000.

Lavrov, A., The Kaiser effect in rocks: principles and stress estimation techniques, *Int. J. Rock Mech. Mining Sci.*, **40**, 151–171, 2003.

Lee, J.-C., Y.-G. Chen, K. Sieh, K. Mueller, W.-S. Chen, H.-T. Chu, Y.-C. Chan, C. Rubin, and R. Yeats, A vertical exposure of the 1999 surface rupture of the Chelungpu fault at Wufeng, western Taiwan: Structural and paleoseismic implications for an active thrust fault, *Bull. Seismol. Soc. Am.*, **91**, 914–929, 2001.

Ma, K. F., J. Mori, S. J. Lee, and S. B. Yu, Spatial and temporal distribution of slip for the 1999 Chi-Chi, Taiwan, earthquake, *Bull. Seismol. Soc. Am.*, **91**, 1069–1087, 2001.

Ma, K.-F., H. Tanaka, S.-R. Song, C.-Y. Wang, J.-H. Hung, Y.-B. Tsai, J. Mori, Y.-F. Song, E.-C. Yeh, W. Soh, H. Sone, L.-W. Kuo, and H.-Y. Wu, Slip zone and energetics of a large earthquake from the Taiwan Chelungpu-fault Drilling Project, *Nature*, **444**, 473–476, doi: 10.1038/nature05253, 2006.

Oglesby, D. D. and S. M. Day, Fault geometry and the dynamics of the 1999 Chi-Chi (Taiwan) earthquake, *Bull. Seismol. Soc. Am.*, **91**, 1099–1111, 2001.

Rau, R. J., F. T. Wu, and T. C. Shin, Regional network focal mechanism determination using 3D velocity model and SH/P amplitude ratio, *Bull. Seismol. Soc. Am.*, **86**, 1270–1283, 1996.

Sato, N., Y. Yabe, K. Yamamoto, and H. Ito, In situ stresses near the Nojima fault estimated by Deformation Rate Analysis, *Zisin 2*, **56**, 157–169, 2003.

Scholz, C. H., Evidence for a strong San Andreas fault, *Geol.*, **28**, 163–166, 2000.

Seno, T., The instantaneous rotation vector of the Philippine Sea plate relative to the Eurasian plate, *Tectonophys.*, **42**, 209–226, 1977.

Song, S. R., L. W. Kuo, E. C. Yeh, C. Y. Wang, J. H. Hung, and K. F. Ma, Characteristics of the Lithology, Fault-related Rocks and Fault Zone Structures in the TCDP Hole-A., *Terr. Atmos. Oceanic Sci.*, **18**, 2007 (in press).

Tanaka, H, W. M. Chen, K. Kawabata, and N. Urata, Thermal properties across the Chelungpu fault zone and evaluations of positive thermal anomaly on the slip zone: Are these residuals of heat from faulting?, *Geophys. Res. Lett.*, **34**, doi:10.1029/2006GL028153, 2007.

Villaescusa, E., M. Seto, and G. Baird, Stress measurements from oriented core, *Int. J. Rock Mech. Min. Sci.*, **39**, 603–615, 2002.

Wu, C., M. Takeo, and S. Ide, Source process of the Chi-Chi earthquake: S joint inversion of strong motion data and Global Positioning System data with a multifault model, *Bull. Seismol. Soc. Am.*, **91**, 1128–1143, 2001.

Wu, H., J. Hung, E. Yeh, and J. Dong, Characters of faults and structures revealed from cores and wire-line logs in Hole-A of the Taiwan Chelungpu-fault Drilling, *Eos Trans. AGU*, **86**(52), Fall Meet. Suppl., Abstract T51D-1309, 2005.

Wu, H., K. Ma, M. Zoback, N. Boness, H. Ito, J. Hung, and S. Hickman, Stress orientations of Taiwan Chelungpu-Fault Drilling Project (TCDP) hole-A as observed from geophysical logs, *Geophys. Res. Lett.*, **34**, doi:10.1029/2006GL028050, 2007.

Yabe, Y., Estimating crustal stresses from inelastic behavior of boring core samples under the uniaxial compression, paper presented in *the 1st Workshop on IODP Physical Property Measurement*, Japan Drilling Earth Science Consortium (J-DESC), Kyoto, Japan, 2004.

Yabe, Y., N. Sato, K. Yamamoto, K. Obara, and K. Kasahara, A new technique to measure crustal stresses based on hysteresis of AE activity during load-unload cycle, *abstract of 2004 Japan Earth and Planetary Science Joint Meeting*, J036-P015, Makuhari, Japan, 2004.

Yamamoto, K., The rock property of in-situ stress memory: Discussions on its mechanism, reported in *Int. W/S on Rock Stress: Measurement at Great Depth*, 8th ISRM, Tokyo, Japan, 1995.

Yamamoto, K., Y. Kuwahara, N. Kato, and T. Hirasawa, Deformation rate analysis: A new method for in situ stress estimation from inelastic deformation of rock samples under uniaxial compressions, *Tohoku Geophys. J. (Sci. Rep. Tohoku Univ., Ser. 5)*, **33**, 127–147, 1990.

Yamamoto, K., H. Yamamoto, N. Kato, and T. Hirasawa, Deformation rate analysis for in situ stress estimation, AE/MS activity, in *Geol. Struct. Mat.*, edited by H. R. Hardy Jr., Trans. Tech. Pub., 243–255, 1993

Yu, S. H., H. Y. Chen, and L. C. Kuo, Velocity field of GPS stations in the Taiwan area, *Tectonophys.*, **274**, 41–59, 1997.

Zeng, Y. and C. H. Chen, Fault rupture process of the 20 September 1999 Chi-Chi, Taiwan, earthquake, *Bull. Seismol. Soc. Am.*, **91**, 1088–1098, 2001.

Zoback, M. D., M. L. Zoback, V. S. Mount, J. S. Suppe, J. P. Eaton, J. H. Healy, D. Oppenheimer, P. Reasenberg, L. Jones, C. B. Raleigh, I. G. Wong, O. Scotti, and C. Wentworth, New evidence on the state of stress of the San Andreas fault system, *Science*, **238**, 1105–1111, 1987.

Y. Yabe (e-mail: yabe@aob.geophys.tohoku.ac.jp), S.-R. Song, and C.-Y. Wang